THREE-DIMENSIONAL TOMOGRAPHY OF INTERPLANETARY DISTURBANCES

Bernard V.Jackson and P.Paul Hick
Center for Astrophysics and Space Sciences, University of California at San Diego, LaJolla, CA, U.S.A.

Received 1 January 2003

Abstract. We have developed a Computer Assisted Tomography (CAT) program that modifies a three-dimensional kinematic heliospheric model to fit interplanetary scintillation (IPS) or Thomson scattering observations. The tomography program iteratively changes this global model to least-squares fit the data. Both a corotating and time-dependent model can be reconstructed. The short time intervals of the time-dependent modeling (to shorter than 1 day) force the heliospheric reconstructions to depend on outward solar wind motion to give perspective views of each point in space accessible to the observations, allowing reconstruction of interplanetary Coronal Mass Ejections (CMEs) as well as corotating structures. We show these models as velocity or density Carrington maps and remote views. We have studied several events, including the July 14, 2000 Bastille-day halo CME and other intervals using archival Cambridge IPS data, and *Helios* photometer Thomson-scattering data. We compare our results with additional remote-sensing observations, and *in situ* observations from near-Earth spacecraft. When heliospheric remote sensing observations (IPS and/or Thomson-scattering) are available in real time, this CAT technique provides a novel method to predict solar wind conditions at Earth at least one day ahead of time. We run one such forecast project based on IPS data received from the Solar Terrestrial Environment Laboratory, Japan.

1. Introduction

In coronal and heliospheric physics there have been numerous attempts to reconstruct the corona and heliosphere in three dimensions. Near the Sun there is good reason to determine the three dimensional shapes of structures in order to learn about their initiation and source of energy. Coronal mass ejections (CMEs) often have a loop-like appearance. As helical loops driven by currents as proposed by Anzer (1978) or Mouschovias and Poland (1978) the shape of a CME should follow a very specific pattern. If, however, a CME is a spherical bubble, then it might very well be the remnant of a large addition of energy at a single point in the low corona (Wu, Dryer, and Han, 1976). Various techniques used to determine CME shapes from the single perspective of Earth, including polarization (Munro 1977; Crifo, Picat, and Cailloux, 1983) and depletion of the corona (MacQueen, 1993) indicate that CMEs are extensive coronal structures. Studies using multiple perspectives from

spacecraft viewing from different vantage points (Jackson *et al.*, 1985) reach the same conclusion. The extent and the shape of structures in of the background corona are also important. For instance, the shapes and positions of coronal streamers indicate their location and extents relative to the magnetic structures on the Sun. This in turn gives an indication of whether all streamers are formed by the effects of a global solar current 'pinch' effect or some more local magnetic phenomena. For studies of the solar wind and the processes that supply its energy, these studies can only be carried out if a global description of the solar wind is available.

Forecasting in heliospheric physics requires remote sensing techniques that determine the three-dimensional and evolving shapes of solar and interplanetary structures. The three-dimensional morphology of solar features allows a determination of whether or not a solar structure will affect Earth. In the case of flares and other large transient changes near the solar surface this information can tell whether that structure will erupt and then whether or not this eruption will affect the Earth. This premise, more than any other, has promoted the three-dimensional observations that will be possible from the two NASA's STEREO spacecraft that are now under construction. When global remote sensing heliospheric data are available, a new type of computer assisted tomography is possible that reconstructs the corotating and outward-expanding solar wind by the rearrangement of features along each line of sight. These ideas follow a lengthy heritage of such analyses.

Tomography is best-known for its application in the medical profession, where it is used as a non-invasive way to probe the human body, and reconstruct its internal structure in three dimensions (Gilbert, 1972). However, one of the earliest uses of tomography was in solar radio astronomy (Bracewell, 1956). Other areas where tomographic reconstruction techniques have been successfully applied are in studies of binary star systems (Marsh and Horne, 1988) and accretion disks in astrophysics (Gies *et al.*, 1994), acoustic sounding in oceanography (Worcester, Corunelle, and Spindel, 1991), seismic studies in geology (Anderson and Dziewonski, 1984), auroral studies (Frey *et al.*, 1996) and coronal studies in solar physics (Hurlburt *et al.*, 1994). An application in atmospheric modeling, somewhat similar to our model in its use of an irregular sampling of refractometric sounding observations is discussed in Gorbunov (1996). In general, depending on the object resolution and noise in the data set, when more perspective views of an object are available, a finer resolution of its three dimensional structure becomes possible. In medical applications it is generally possible to obtain many views from as many different directions as deemed necessary. Most other tomographic applications are limited in the ability to view

objects from a large number of directions. However, depending on the choice of orientation and resolution of the three dimensional matrix shape relative to the input images, even a single perspective view can provide a unique solution for an object's three dimensional structure (Katz, 1978).

Some of the first coronal tomographic analyses from Skylab coronagraph observations (Wilson, 1977; Jackson, 1977) used solar rotation to provide perspective views of the corona. Coronal tomography has been enhanced recently by Zidowitz, Inhester, and Epple (1995) using rotational tomographic techniques to reconstruct coronal densities from Mark III coronagraph observations. Corotational tomography of SOHO UVCS data (Panasyuk, 1999; Frazin, 2000; Frazin and Jansen, 2002) has shown considerable improvement over techniques that simply assume the structure is on the limb at the time of observation. A two-perspective view tomography analysis of CMEs by Jackson and Hick (1994) and Jackson and Froehling (1995) performed using Solwind coronagraph and *Helios* spacecraft photometer observations show the extended three dimensional shape of two CMEs.

Since the 1960's interplanetary scintillation (IPS) measurements have been used to probe solar wind features with ground-based meter-wavelength radio observations (Hewish, Scott, and Wills, 1964; Houminer, 1971). Scintillation-level intensity IPS observations, which arise from small-scale ($\sim$200km) density variations, highlight heliospheric disturbances of larger scale that vary from one day to the next and are often associated with geomagnetic storms on Earth (Gapper *et al.*, 1982). These 80 MHz scintillation-level IPS observations show a predominance of disturbances that appear to corotate with the Sun as inferred from a list of events, their shapes, and their solar surface associations (Hewish and Bravo, 1986). Observations from the UCSD (Coles and Kaufman, 1978) and Nagoya (Kojima, and Kakinuma, 1987) multi-site scintillation array systems have been used to determine velocities in the interplanetary medium since the early 1970's.

Significant results have been obtained from IPS remote sensing observations even when using a rudimentary determination of the location of solar wind structures, *i.e.*, the assumption that all material is present at the location of closest approach to the Sun long each line of sight. For instance, from IPS velocity data it was determined that the polar solar wind has high speed (Kakinuma, 1977; Coles, *et al.*, 1980; Kojima and Kakinuma, 1990) long before observations from the Ulysses spacecraft (McComas *et al.*, 1995) measured these velocities *in situ*. Regions of slow solar wind are generally found near the solar equator especially at solar minimum, and thus near the location of the magnetic neutral line as determined by the potential magnetic field model (Hoeksema,

Wilcox, and Scherrer, 1983). Scintillation level data from the Cambridge scintillation array have been analyzed in the same manner (Hick *et al.*, 1995). The Carrington maps produced by this technique show that the solar polar regions generally do not scintillate very strongly compared to regions near the solar equator. Houminer and Gallagher (1993) find that some of the regions which scintillate strongly and corotate or return from one rotation to the next are located near the heliospheric current sheet as defined by the potential field model. Hick *et al.* (1995) have determined that solar active regions generally bright in X-rays, and not the current sheet, are the solar surface locations of most corotating regions observed to scintillate strongly in the Cambridge IPS observations.

Heliospheric tomography of transient heliospheric structures using global IPS data has often been attempted without the aid of sophisticated computer techniques. These analyses (Gapper *et al.*, 1982; Behannon, Burlaga, and Hewish, 1991) have relied on a combination of solar rotation, outward motion and *in situ* observations to determine the three dimensional extent of coronal structures. In these analyses, models of different three dimensional coronal structures were used to determine their appearance on a two dimensional image "template". The two dimensional templates were then matched by eye to the observed image to select one of the models best representing the data. A more sophisticated approach to this same idea has been pursued by Tokumaru *et al.* (2002) and Hayashi *et al.* (2002) who fit assumed model structures to data from one day's observation of IPS data.

The techniques described here apply computer assisted tomography methods to data primarily obtained from one location in space. The corotational analyses (Jackson *et al.*, 1997b; 1998; Kojima *et al.*, 1997; 1998; Asai *et al.*,1998; Jackson and Hick, 2002) using these techniques improve upon the inherent averages made by assuming all material lies at the point of closest approach of the line of sight to the Sun. IPS and Thomson scattering observations covering a large range of solar elongations (angular distances from the Sun) and obtained over an extended period of time provide a global view of the inner heliosphere, and both solar rotation and outward solar wind motion provide multiple perspectives required for tomographic analyses. Selecting observations from a quiet part of the solar cycle as structures rotate during the period of observation can minimize effects due to their evolution. Iterative tomographic methods can be used to find a three dimensional heliospheric model of these density variations, producing line-of-sight integrated model IPS observations matching the actual IPS observations as nearly as possible. A time-dependent version of this tomographic technique from a single point in space (as in Jackson, Buffington and Hick, 2001;

Jackson *et al.*, 2002; Jackson, Hick, and Buffington, 2002) relaxes the assumption that heliospheric structure remains constant over time. In this newest technique, a global kinematic model is formed at regular time intervals, and the iterative process provides the three-dimensional heliospheric parameters that fit observed data. These analyses allow short temporal variations in the data to be reconstructed. Due to the shortness of these time steps, perspective views of the data come from outward motion of solar wind plasma, and not solar rotation.

The next section gives a background for both the global IPS and *Helios* photometer Thomson scattering observations that have inspired these tomographic techniques. The third section describes the solar wind model used and the tomographic program that has been developed to fit this model. The forth section shows that the solar wind model derived from the remote sensing data indeed reproduces the original observations. The fifth section compares the tomographic models to *in situ* data from Earth and in the Thomson-scattering analysis, *Helios* spacecraft density data. The sixth section displays and discusses the kinematic model values in a variety of ways including remote observer views of the data and as Carrington synoptic maps. We conclude in the last section.

2. Global Data Analyses

The IPS technique relies on several assumptions to relate changes in scintillation level and velocity integrated along each line of sight to local changes in the scintillation level and velocity. In weak scattering (assumed here exclusively) the Born approximation holds, and the scintillation pattern at Earth is a sum of contributions from each thin scattering layer perpendicular to the line of sight (Tatarski, 1961). At any given radio frequency the weak scattering approximation breaks down at solar elongations close to the Sun, and IPS observations are no longer optically thin. This effect provides an effective limit to IPS observations close to the Sun. This limit depends on observing frequency and radio source size.

Heliospheric Thomson scattering (photospheric sunlight scattered from electrons) present along each line of sight, on the other hand, is optically thin to elongations from within a small fraction of a solar radius out to 180°. Unlike ground-based interplanetary scintillation measurements, Thomson-scattering brightness is only a tiny component of the total observed heliospheric signal. At elongations of a few degrees Thomson scattering brightness is at best only a few percent of the zodiacal light, and this percentage becomes less at even greater

elongations. Stellar signals can also be hundreds of times brighter than those from heliospheric Thomson scattering. From the surface of the Earth mesopheric air glow at even the darkest sites presents a time-variable signal that is several tens larger (Garcia, Taylor, and Kelley, 1997; James *et al.*, 1997) than heliospheric signals. Mesospheric air glow has effectively limited ground-based Thomson scattering observations to elongations within a few solar radii of the Sun and the best of these are obtained at times of total solar eclipses by high-flying aircraft (Chapman, 1979).

The tomographic program employed here requires that the contribution of a solar wind model be estimated along each line of sight. The model is iteratively changed to fit observations by following contributions from segments along a line of sight back to its origin on an inner boundary and formally inverting the contributions to this inner boundary according to weights assigned to each line of sight segment. The contribution of each line of sight segment to the integrated line of sight value is determined from the solar wind model. The inner boundary or source surface makes the tomographic inversion a two dimensional problem, thus maximizing the information from each line of sight observation. The weight for each line-of-sight segment consists of a part determined from the IPS or Thomson scattering process itself and a part determined from the solar wind (*i.e.*, local density or velocity). The following two subsections give line of sight weighting details for IPS g-levels, velocities, and Thomson-scattering brightness.

2.1. IPS Measurements

Scintillation-level measurements are available from 1990 through September 1994 from nearly 1000 sources observed daily at 80 MHz by the Cambridge array telescope. In recent years radio source scintillation-level observations have been obtained from several tens of sources measured each day by the the group at the Solar-Terrestrial Environment Laboratory (STELab), Toyokawa City (Nagoya University), Japan. These observations have been available from the STELab radio telescope at Kiso from 1997 to the present and more recently (since mid-2002) from the STELab radio telescope at Fuji. The IPS analysis shown here uses data from relatively short time intervals from the Cambridge, England and STELab telescopes in 1994 and from STELab during July 2000. The disturbance factor g is defined as

$$g = m/ < m >, \tag{1}$$

where m is the observed fractional scintillation level $\Delta I/I$, the ratio of source intensity variation to intensity and $< m >$ is the modeled mean

level of $\Delta I/I$ for the source at the elongation at the time of observation. Scintillation level measurements from the STELab radio facility analyses are available at a given sky location as an intensity variation of the source signal strength. For each source, data are automatically edited to remove any obvious interference discerned in the daily observations. To obtain the scintillation index m in real time, the white noise P_{WN} is subtracted from the scintillation signal spectrum $P(f)$, and then system gain corrections are determined by automatically calibrating with the white noise level at the high frequency end of the power spectrum.

$$m = \int (P(f) - P_{WN})/P_{WN} df. \tag{2}$$

For real-time processing at UCSD the mean scintillation index $< m >$ is determined from a least-square fit of m as a function of source elongation (ignoring the dependence of position angle). We require that a minimum of 8 daily measurements is needed to calculate $< m >$. The real-time g-level is the ratio of the daily m and the least-square-fit value $< m >$.

The weight factor along the line of sight $W_I(s)$ can be approximated for IPS in weak scattering (Young, 1971) at the 327 MHz frequency of the STELab IPS observations and at the 80 MHz frequency of the Cambridge, England array as

$$W_I(s) = 2\pi \int sin^2 \left(\frac{q^2 \lambda s}{4\pi} \right) exp \left(-\frac{\theta_0^2 q^2 s^2}{2} \right) q^{-3} dq. \tag{3}$$

In this general IPS weight integral, q is the wave vector. We use a single power law for the spectrum, the same for slow and fast solar wind, with an average power index of 3. The average angular size of a radio source is set at $\theta_0 = 0.3$ arc sec at the wavelength $\lambda = 3.68$ m (81.5 MHz) of the Cambridge IPS observations and at $\theta_0 = 0.1$ arc sec at the wavelength $\lambda = 0.917$ m (327 MHz) of the STELab IPS observation. These weights are plotted in Figure 1. The scintillation level m is related to the small-scale density variations along the line of sight by

$$m^2 = \int \Delta n_e(s)^2 W_I(s) ds. \tag{4}$$

Here, $\Delta n_e(s)$ are the small-scale density variations at distance s along the line of sight. We assume that the small-scale variations scale as a power law of the heliospheric density and heliocentric distance,

$$\Delta n_e = A_C R^{PWR} n_e^{PWN}, \tag{5}$$

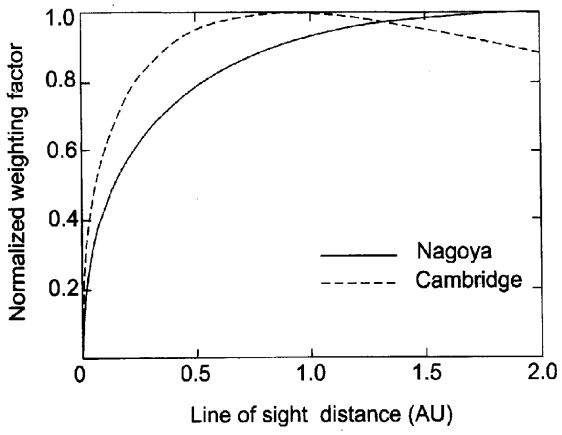

Figure 1. Normalized weighting functions for Cambridge and Nagoya interplanetary scintillation (IPS).

where A_C is a proportionality constant, PWR is a power of the radial falloff (Asai *et al.*, 1998) and PWN is the power of the density. In the present analysis, the program fits the values of PWR and PWN to best fit the data over the interval chosen. For instance, for the time period presented for the Bastille-day CME using Nagoya data, A_C is set equal to 1 and the two powers PWR and PWN are -3.5 and 0.7, respectively, to best fit *in situ* density over a ten-day time interval centered on the time the Bastille-day CME reaches Earth. These constants depend to some extent on the model used as the mean value of $< m >$ of a source with elongation at various frequencies used to determine g-level. Constants with comparable values are used to fit the *in situ* data for the 80 MHz Cambridge scintillation-level measurements for given time intervals.

Generally, valid IPS velocity data from the Nagoya scintillation arrays are available from the same radio sources as observed in scintillation level each day. IPS velocities, based on observations from up to four scintillation arrays operated by STELab, Japan, have been available since 1985. Our tomography program assumes that IPS velocity follows a similar line of sight weighting as the intensity scintillation, and the powers PWR and PWN are assumed to be the same for the STELab velocity and g-level measurements. The velocity correlation is not very sensitive to differences in these two power functions. Thus, when IPS velocities (from Nagoya) are combined with Cambridge g-level data, constants PWR and PWN for the velocities are taken from best fits

during other time intervals where Nagoya g-level data is present, while constants for the Cambridge g-levels needed to relate to density are determined to best fit the current data. We approximate the velocity observed at Earth as in Jackson *et al.*, 1998 (see Kojima *et al.*, 1998, for a more complete formulation and validity tests) as the weighted integral,

$$V = \frac{\int V_{\perp}(s)\Delta n_e(s)^2 W_N(s) ds}{\int \Delta n_e(s)^2 W_N(s) ds)}, \tag{6}$$

where $V_{\perp}(s)$ is the component of the solar wind velocity perpendicular to the line of sight. The quantity $\Delta n_e(s)$ is the small-scale electron density variation at distance s along the line of sight as determined by the level of intensity scintillation, and the weighting factor W_N for the STELab observing frequency is used.

The IPS data is extensively edited using a variety of techniques before it is used in the tomographic analysis. The Cambridge, England 80 MHz source observations are in weak scattering beyond about 30° elongation and are not used in the analysis at elongations less than this. For these g-level data considerable attention was paid to the removal of ionispheric scintillation, resulting in the elimination of all data at greater than 80° elongation, primarily because ionispheric scintillation at a single radio site at this radio frequency is difficult to detect in the scintillation-level data automatically. Further, solar radio noise was sometimes detected as a band of higher noise at one hour angle (that corresponded to a single time) in Cambridge data. When this noise level was suspected, the data for this entire time was eliminated. In all about 10% of the data between 30° and 80° elongation was eliminated in the Cambridge data. Even more extensive editing procedures, developed and refined over many years of data taking at STELab, have been largely computerized so that man-made, solar, ionispheric scintillation, and other natural (*i.e.*, lightening) noise sources are removed as completely as possible from the final STELab data set. At UCSD we only use STELab velocity and g-level data from elongations greater than 11.5° to insure that the radio source lines of sight are in the weak scattering regime. Currently, scintillation-level data are available from two of the STELab radio arrays, at Kiso and Fuji in Japan. At UCSD we analyze both of these data sources independently for g-level as described above, and then choose the lower of the two g-level values for use in the tomography analysis if measurements exist for the same source from the two stations.

2.2. *Helios* Spacecraft Thomson Scattering Measurements

The *Helios* spacecraft, launched in December 1974 (*Helios* 1) and January 1976 (*Helios* 2), each contained three zodiacal-light photometers which were originally intended to measure the distribution of dust in the interplanetary medium between the Sun and the Earth (Leinert *et al.*, 1975, Leinert, Link, and Salm, 1981). However, these photometers also measured brightness variations produced by Thomson scattering from large-scale structures in the interplanetary electron density. The three photometers were fixed on the spacecraft and rotated at its 1 s spin period on an axis perpendicular to the plane of the ecliptic; they pointed 16°, 31° and 90° south (*Helios* 1) or north (*Helios* 2) of the ecliptic plane. Data from the 16° and 31° photometers were binned into 32 longitude sectors at constant ecliptic latitude around the sky. The data were integrated over 8.6-min periods in turn from each of the three photometers, through a set of broad-band ultraviolet, blue, and visual light filters and a set of one clear and three polarizing filters, with a time interval of about five hours between the same combination of color and polarization filters. All *Helios* photometer data are available from the National Space Science Data Center (NSSDC).

Richter, Leinert, and Planck (1982) first described use of these data to follow plasma ejections detected by Thomson scattering out to 90° solar elongation. Since then Jackson and Leinert (1985) and Jackson (1985) used these data to study characteristics of mass ejections and trace their motion outward from the Sun into the anti-solar hemisphere (Figure 2). Jackson (1991) also used these data to study the longer-lasting corotating regions in the solar wind. The *Helios* spacecraft orbited the Sun between 0.3 to 1 AU with 6-month periods, and its photometers viewed heliospheric structures from a non-Earth location. Interpretation of these observations must take this non-Earth viewpoint into account to match observed brightness to heliospheric structure.

Line-of-sight Thomson-scattering brightness for a column of electrons follows the relationship,

$$B = \int n_e(s) W_T(s) ds, \tag{7}$$

where $n_e(s)$ is the electron density per cm^{-3}, at distance s in cm, along the line of sight; $W_T(s)$, the scattered intensity per electron, serves as a brightness 'weight factor' for the density. For the large elongations from the Sun viewed by the *Helios* photometers,

$$W_T(s) = \frac{1}{2}\sigma F_s \left(\frac{r_0}{r}\right)^2 (2 - \sin^2\chi), \tag{8}$$

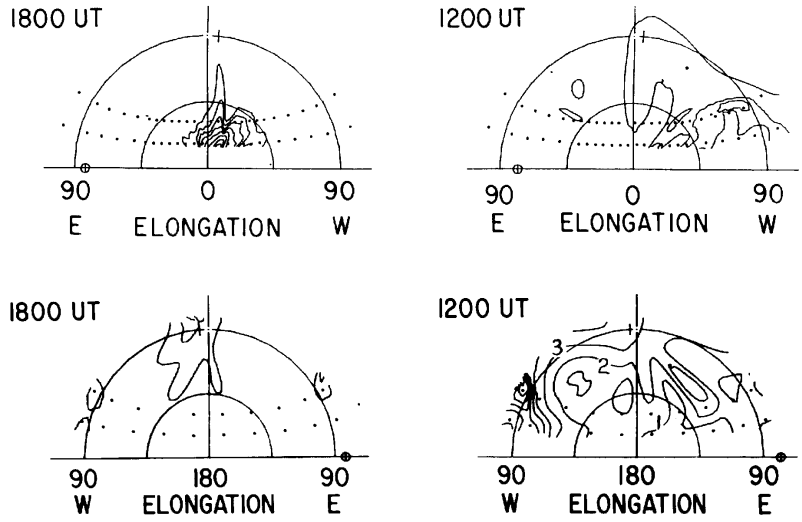

Figure 2. Contour plot images obtained from the *Helios* photometers of the May 7, 1979 CME on May 8 and May 9 at the times indicated. In the top two images the Sun is centered and 90° marked as the outer semi-circle above the ecliptic plane (represented by the horizontal line). Electron contour density is plotted in levels of 3×10^{14} e$^-$ cm^{-2} The position of the Earth is marked as $\oplus$ near east 90° Positions of the sector centers are marked by dots. The bottom two images view directly away from the Sun and are contoured in levels of 10^{14} e$^-$ cm^{-2}.

where σ is the Thomson-scattering cross section, F_s is the flux received from the solar disk at a distance r_0, r is the distance of the electron from the Sun, and χ is the angle between the incident solar radiation and the direction of scattering (Billings, 1966). To evaluate Eq. (8) both r and χ are determined as functions of the distance R of the observer from the Sun, elongation ϵ of the line of sight, and distance s along the line of sight. Using R, ϵ and s as independent variables W_T scales as R^{-2}. For a fixed R and ϵ the function W_T has a maximum at $s = R\cos\epsilon$, and is symmetric around this point. For ϵ<90° the maximum is at the point of closest approach of the line of sight to the Sun. Figure 3 shows the weight function at $\epsilon = 16°$, 31° and 90° for $R = 1$ AU.

Helios photometer brightness data are usually specified in S10 units, the brightness within one square degree of sky scaled to the equivalent brightness of a tenth-magnitude solar-type star. Expressing Eq. (7) and Eq. (8) in S10 units requires that the flux F_s received from the Sun [Eq. (8)] also be specified in S10 units:

$$\frac{1}{2}\sigma F_s = \frac{1}{2}\sigma(\Delta\Gamma/\Omega_s)10^{(10-m)/2.5}, \qquad (9)$$

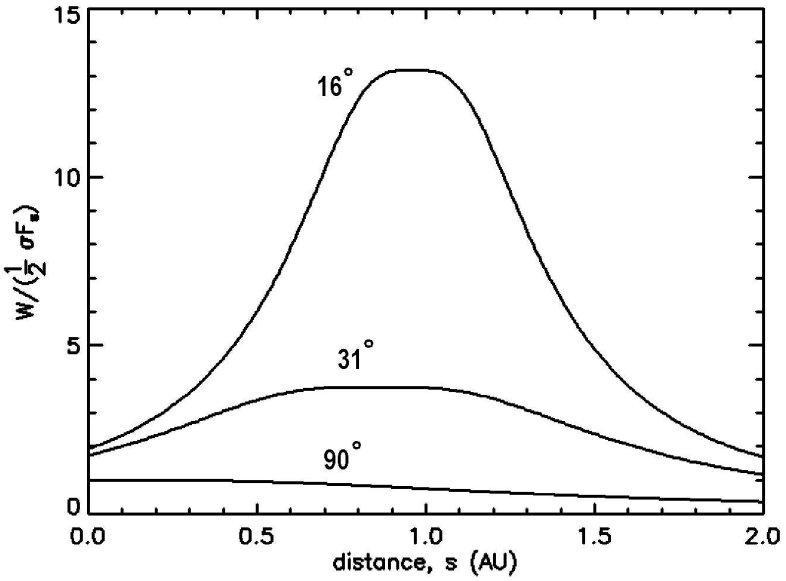

Figure 3. Thomson-scattering weight function W from Eq. (8) as a function of distance s along the line of sight for the elongations given. The observer is assumed to be at $R = 1AU$ from the Sun.

where $\Delta\Gamma = 3.046 \times 10^{-4}$ is the solid angle in steradians subtended by one square degree, and Ω_s and m are the solid angle and apparent magnitude of the Sun, respectively. These quantities, at 1 AU are $m = -26.73$, $\Omega_s = 6.800 \times 10^{-5}$ (Allen, 1964) and thus,

$$\frac{1}{2}\sigma F_s = 8.76 \times 10^{-11} cm^2 S10. \tag{10}$$

The data from the *Helios* photometers is brightness time-series information in heliocentric coordinates mapped relative to the Sun. These time series (see next section) have had a zodiacal light model (Leinert *et al.*, 1981) removed and stellar signals eliminated. To further refine these time series for use with the tomography, we remove an 8-day running mean. This filter removes a portion of the low-frequency response not otherwise accounted for. At this level, the *Helios* systems act as differential photometers for high-frequency heliospheric signals. In addition, the final time series is searched for "glitches". These generally appear as spikes in the data that are more prominent above the background in the direction opposite the Sun. These spikes are often correlated with high-energy particle flux observed in the *Helios* particle detectors (Jackson and Hick, 2002). When these spikes are detected in the photometer data, the whole period of time from the *Helios* photometers is

considered suspect and is eliminated from consideration even though the high-energy particle spike is not prominent in the photometer observations nearer the Sun. The *Helios* photometer observations get no closer than within 15° from the Sun, and from the innermost orbital position of the *Helios* spacecraft (0.3 AU) this amounts to a closest approach distance of ∼17 solar radii.

Because the heliospheric time series signal is inseparable from the very bright zodiacal light component except by its rapid (less than ∼8-day) variation over time, the tomographic analysis must deal with the fact that there is a steady background Thomson-scattering signal component as well as the time-varying one. Several techniques have been devised to include an estimate of this signal in our Thomson-scattering analysis. One of the first methods was to simply analyze the variations relative to the 8-day running average (Jackson and Hick, 2000; 2002). After the 3-D analysis was complete, a small additional r^{-2} density was added to the data to provide a total density at 1 AU commensurate with the mean value for that time interval at Earth. In the current tomographic analysis shown here, an additional r^{-P} background density with a constant value at 1 AU is added to the model data prior to the tomographic analysis. The sum of the modeled background brightness and the observed variable component are now compared with total modeled brightness from the three-dimensional model. The *Helios* spacecraft densities (rather than those at Earth) are now also compared over the time interval in question with the densities derived from our model in order to provide a best fit to the value of P and the density at 1 AU. For the period of time during May 1979, P was found to be 2.07 with a density at 1 AU of 7.0 e^- cm^{-2}. For a less active time in 1977 (Carrington rotation 1653) P was found to be $\approx$2.10 with a 1 AU value of 8.5 e^- cm^{-2}. The different techniques used in background density fitting make little difference in the location of the heliospheric structures reconstructed, but they do somewhat change the overall density.

3. Model and Tomographic Analysis

The heliospheric model in our analysis and the iterative procedure that provides the three-dimensional results are explained more thoroughly in Jackson *et al.* (1998). The UCSD tomography program currently applies corrections to a kinematic solar wind model until there is a least squares best fit match with the observations. The solar wind model contains two plasma parameters which are fit in three dimensions: the radial solar wind velocity and the solar wind density. Model line of sight

observations are obtained by integrating through the solar wind model. For the IPS analysis the small-scale density variations are obtained from the solar wind density power law equations; the perpendicular solar wind component $V_\perp$ follows from the radial solar wind speed using the line of sight geometry. In the Thomson scattering case, density is used directly in the line of sight integral (Eq. 7).

3.1. Solar Wind Model

The three-dimensional solar wind is currently constructed by projecting it outward from a source surface below the lowest lines of sight, and unlike the UCSD model described in Jackson *et al.*, 1998 where this surface was placed at 0.3 AU. Consistent approximately with *in situ* spacecraft observations (Hundhausen *et al.*, 1970), the solar wind motion is assumed to be strictly radial, and thus, for example, faster solar wind catches up with slower wind. After merging the solar wind speed follows by assuming mass flux conservation of the plasma within the latitudinal band resolved by the model. At each heliocentric distance and especially at the source surface, the velocity structure of the model is smoothed so that some information from neighboring latitudes and longitudes is retained. The smoothing incorporates adjacent pixels in the map using a Gaussian filter weighted according to the angular distance of the adjacent resolution elements at the same heliocentric distance. This Gaussian filter is usually set with a 1/e value of about 0.75 of the latitude spatial digital resolution interval. Since the resolution of a rectangular Carrington coordinate map increases spatially in longitude with increasing latitude, this filter is used to even the spatial resolution over the whole of the map.

In the kinematic model described here, we either assume that the solar wind corotates so that for the period of observation there is no temporal variation (other than rotation) or else that the source surface boundary can change over evenly spaced time intervals. This latter time-dependent tomography allows changes at the source surface boundary over time scales shorter than one day. The corotation assumption allows robust tomographic convergence when the numbers of lines of sight are small and when the data are noisy. The time-dependent assumption requires less noisy data and more lines of sight to provide the same spatial resolution, but essentially limits the tomographic reconstruction to rely on outward solar wind flow to form the perspective views. For each observed line of sight at a given time, the location of the position along this line in the model is calculated. The model g-levels along each line of sight defined by the densities are summed using the weighting described in Eq. (3) or in the case of the Thomson scattering

data, by the weighting described in Eq. (8). These model values are then compared with the observed g-levels, or brightness and this comparison is used to change the solar wind model. For one solar rotation of Nagoya STELab data there are typically between 500 to 1000 lines of sight available. This implies that for STELab data between 20 and 40 lines of sight input to latitude and longitude positions each day subject to the Gaussian spatial filter described earlier, and a similar Gaussian filter that combines data from one day to the next. This implies a possibility of determining the density/g-level values for 20 to 40 latitude and longitude locations and a similar number of velocity latitude and longitude locations from STELab data each day. The Cambridge IPS lines of sight are as numerous as several hundred per day as are the Thomson scattering data from each *Helios* spacecraft. These greater line of sight numbers can in principle provide better temporal and spatial resolution in density.

The quality of the available observations and the heliographic coordinate resolution and temporal data cadence also dictate the resolution. For corotational IPS tomography the STELab data can be resolved with at least 10° by 10° heliographic latitude and longitude digital resolution as can the Thomson scattering data from the *Helios* photometers. For the UCSD time dependent tomographic program using STELab data, 20° by 20° heliographic latitude and longitude digital resolution is used. For the Cambridge and *Helios* photometer data 10° by 10° heliographic latitude and longitude digital resolution has also been used for the time-dependent tomography. This resolution is modified by the Gaussian spatial and temporal filters that limit structure extent in latitude, longitude and (in the case of the time-dependent tomography) height commensurate with the data amounts and quality. In practice it is important that the lines of sight used to determine the value of each resolved point within the model cross each other at different angles and from different elongations. The regions near the Earth are those most frequently crossed by different lines of sight while those far from it, especially over the solar poles, are not. Where the computational aspects of the tomography differ from those given in (Jackson *et al.*, 1998) they are discussed further in the following sub-section.

3.2. Computer Analysis

As in Jackson *et al.* (1998) the computational aspects of the tomography program necessarily deal with the detailed geometry for each line of sight, the location of each within the three-dimensional solar wind model and its projection to the heliocentric source surface. In the tomographic analysis used here, the Carrington map at a given

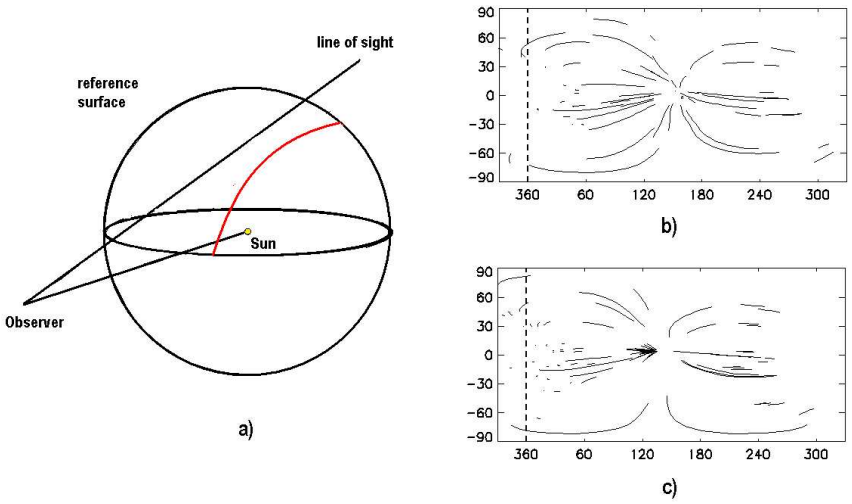

Figure 4. **a)** Schematic of a line of sight and its projection to a constant heliocentric distance here shown as a reference surface below the line of sight. The reference surface is set so that all lines of sight are above it. The curved line below the line of sight on the reference surface is the line of sight projection after taking outward solar wind motion into account. **b)** and **c)** Consecutive-day (July 13 and July 14, 2000) latitude and longitude line of sight projections onto the source surface. Lines of sight are depicted which begin near the Earth and extend outward from it for 2 AU. Different perspectives are obtained where the lines of sight cross and as the weights of the different line segments indicate.

reference surface below all of the lines of sight determines the three dimensional velocity and density model used for the line of sight calculations. In the corotational tomography only a single reference is provided. In the time-dependent tomography a new reference surface is provided at evenly spaced time intervals. A line of sight projects to a given heliocentric distance at a given time as shown in Figure 4 for several STELab IPS Carrington maps during the Bastille-day CME. Lines of sight segments from different elongations and position along a line of sight and different time project to a location on a given reference surface. In addition to the weight factor discussed in Section 2, each segment projection carries along with it the ratio of model and actual observation for the line of sight to which it belongs. The weights and ratios are accumulated for each position on the reference surface, and are then used to calculate corrections to the solar wind model at the source surface. Once these corrections have been applied, a new three-dimensional solar wind is calculated to start the next iteration. The size of the corrections to the source surface and the differences between model and actual observations are used to monitor convergence.

In the tomographic analysis used here, after all lines of sight have been projected onto the source surface the velocity corrections are applied first. Then the three dimensional model is updated and the recalculated lines of sight are projected to the source surface again. This is done to assure that the newest values of velocity and density from the assumption of mass continuity are used to determine the small-scale density variations along each line of sight. Finally, the density corrections are made on the source surface and the three dimensional model is again updated, unlike the earlier scheme reported in Jackson *et al.* (1998) where only one update of the model is made per iteration. We require that more than one line of sight crosses within each digital ($20^\circ \times 20^\circ$ for STELab IPS) heliographic spatial interval for changes to the source surface be made at that position. The number of line of sight crossings are given by an accumulated average of all contributions as derived from the two (space and time) Gaussian filters used. For completeness in the next generated three-dimensional solar wind model, where the sum of all contributors are less than one these locations in the source surface are filled by interpolation from locations where the data can be changed. However, in the final result the coordinate positions that cannot be changed are left blank. The reference surface maps are smoothed each iteration using a Gaussian spatial filter that incorporates equal solar surface areas and a Gaussian temporal filter. These spatial and temporal filters can be varied to insure convergence. Large changes to the filter values have a significant effect on the result. These spatial and temporal filters can be varied to insure convergence when the data are noisy, but (for instance) were set to a 1/e width of 13.5° and 0.85 days, for the $20^\circ \times 20^\circ$ spatial resolution and 1-day model digitization, respectively, during the time intervals shown here for the July 14, 2000 time period using STELab data.

The tomography program (written in Fortran) iterates to a solution, generally converging to a slowly changing model within several iterations. For a typical rotation, a set of velocity and density iterations generally takes about five minutes on a 2.4 GHz Pentium IV computer using 20° by 20° resolution digitization. The UCSD tomography program operates for 9 iterations to be certain the program has converged. At that point source observations for which the model to observed ratio is more than three sigma away from the average are removed from the data. This same criterion is also used to remove daily g-level or Thomson-scattering data that vary beyond the three-sigma limit. The program is then allowed to operate for another 9 iterations. Convergence is monitored using techniques as described in Jackson *et al.* (1998). Tests of the program show that the model solutions are not sensitive to the starting input model, and that after a few iterations

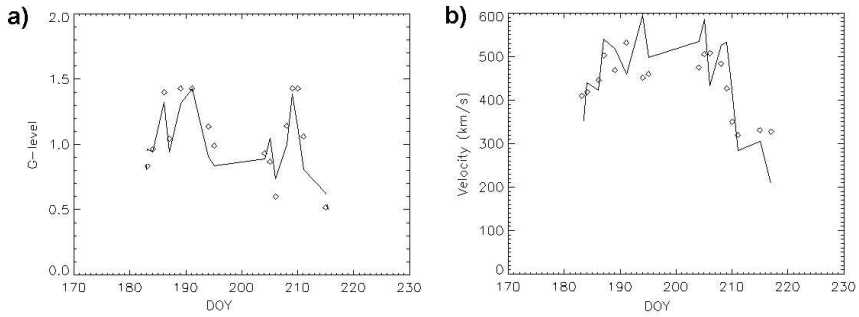

Figure 5. Time series showing a sample of the final (18^{th} iteration) velocity **a)** and g-level **b)** model (open circles) and observations (solid lines) for a time-dependent tomographic run for 48 days from in June-July, 2000 that includes the Bastille-day CME event. The model fits data from radio source 3C161 that was located at 33° elongation one hour west of the Sun on July 14, 2000 (DOY 196). There were a total of 46 radio sources fit in velocity and density during this time interval.

any signature of the input model is lost. Other tests (see Jackson *et al.*, 1998) show that pseudo observation inputs to the three-dimensional model can be reproduced in the tomography.

That the models reproduce the velocity and g-level data are shown in Figure 5 and *Helios* brightness is shown in Figure 6. The data points show a sample time series of the observations for an IPS radio source in velocity and g-level compared with the model values obtained using the UCSD kinematic model after 18 program iterations. Except that the data from some sources are missing on some days, during this time interval the time series for over 50 sources were fit simultaneously in both velocity and g-level in the STELab IPS tomography. For the *Helios* Thomson scattering observations, 130 sky position photometer values obtained approximately every 5 hours (some locations and times are missing from these analysis) were fit simultaneously over the 48-day time period.

The model currently fits all sources with equal weight. Other sources within the same time interval contribute to the model and are the main reason for the discrepancy between the actual and the model values for the specific source shown. An idea of how well the model reproduces the global structure can be gotten simply by a comparison of the individual model values with the data points shown in the IPS velocity and g-level Figure 5 example during June - July, 2000 and in the Figure 6 *Helios* spacecraft photometer brightness sample.

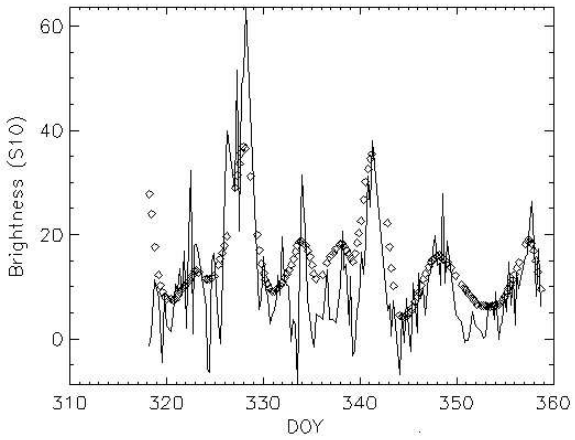

Figure 6. Time series showing a sample of the final (18^{th} iteration) model and photometer brightness comparison for a time-dependent tomographic run for *Helios* November, 1977 data. The observed brightness is shown as a solid line; the model brightness as open circles. The *Helios* 2 16° photometer observations viewing 2° west of the Sun-spacecraft line is shown. November 24 is DOY 328.

4. *In situ* Comparisons

Tomographic model densities and velocities are available in three dimensions and can be extrapolated to any heliocentric distance, for example to 1 AU. These compare directly to *in situ* observations from *e.g.* the Advanced Composition Explorer (ACE) spacecraft near Earth (see Figure 7). We smooth the ACE data into 18-hour averages, consistent with the longitudinal and temporal binning of the time-dependent tomography. The time series are fit by varying the two powers PWR and PWN for Eq. (5) and the spatial and temporal Gaussian filters as mentioned earlier. The densities mapped to 1 AU are shown as a time series for rotation 1965. The correlation for rotation 1965 in model to ACE *in situ* values is 0.82 and 0.85 respectively for velocity and density over the 10-day period centered on the Earth arrival time of the July 14 CME (Figure 7). For IMP *in situ* data fits to the corotational tomography model using Cambridge, England IPS data and STELab IPS velocity data that are not as good as these see the analysis by Jackson *et al.* (1998).

Tomographic time-dependent modeling of Thomson-scattering brightness also allows heliospheric density to be extrapolated to any location in space. The *Helios* spacecraft *in situ* monitors regularly measured proton density, and by assuming that there is one electron present per proton, can be compared with the electron densities derived from the

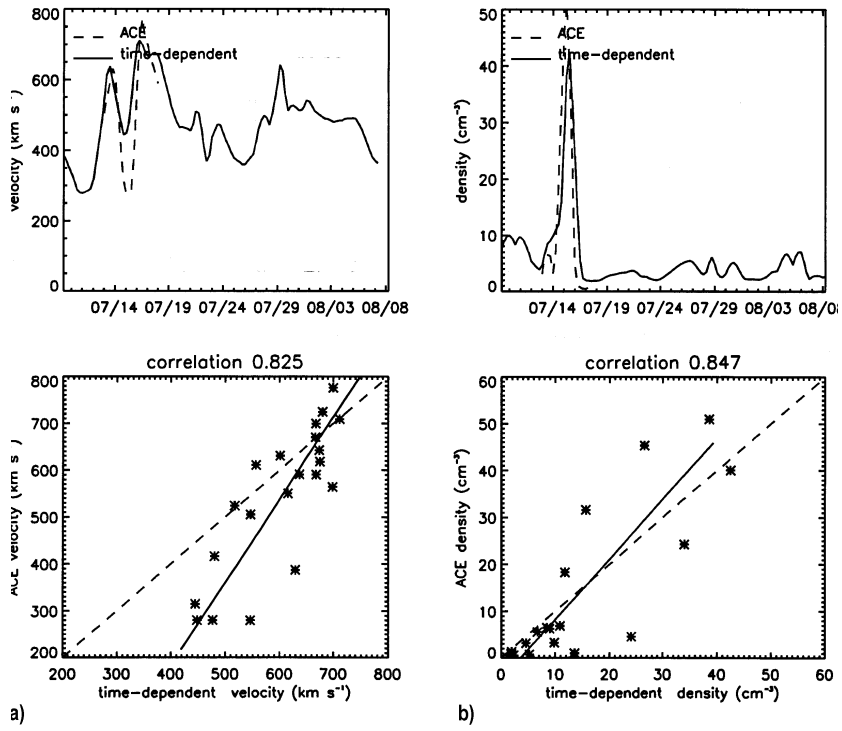

Figure 7. Rotation 1965. **a)** 10-day velocity time series from the three dimensional time-dependent model projected to 1 AU compared to the velocity time series from the ACE spacecraft (dashed line) and its correlation. **b)** Model and ACE density correlation.

tomography. Figure 8 is a comparison plot of heliospheric density at the *Helios* 2 spacecraft and the reconstructed density from the time-dependent kinematic model using *Helios* 2 data only, extracted at the location of the spacecraft during April and May, 1979 (see next section). The *in situ* density values at *Helios* 2 are again averaged using an 18-hour filter consistent with the spatial and temporal resolution of the tomography. The only adjustments allowed in the density tomography model are changes in the Gaussian temporal and spatial filters and an adjustment of the non-varying background heliospheric density component. Even better correlations are possible between model and *in situ* density (Jackson, Buffington, and Hick, 2001) when both *Helios* spacecraft are used to reconstruct the three-dimensional density.

Once a three-dimensional result is available, it can be viewed from any perspective or extrapolated to any position in space with the most accurate values present presumably where data coverage is most

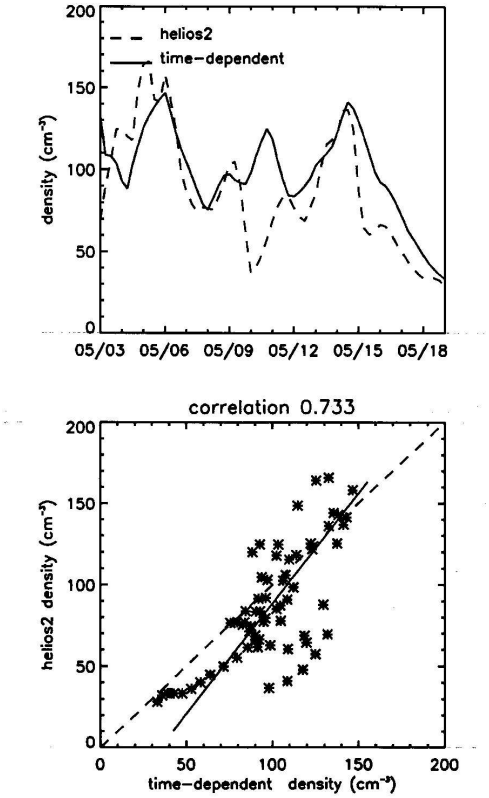

Figure 8. Comparison plot of heliospheric densities at the *Helios* 2 spacecraft and least squares correlation.

complete with the greatest signal relative to the many sources of observational noise. These tomographic reconstructions are shown as Carrington plots at a given height and as remote-observer views in the next section.

4.1. Reconstructed Global Observations

The fits to *in situ* observations only guarantee that the three-dimensional model constructed remotely by the IPS and Thomson scattering analysis over a large portion of the heliosphere agrees with *in situ* data near Earth or, when observations exist, at the *Helios* spacecraft. However, we can also view the reconstructed time-dependent model shapes for these events and see if they match remotely sensed data from other instruments including coronagraph observations obtained closer to the Sun.

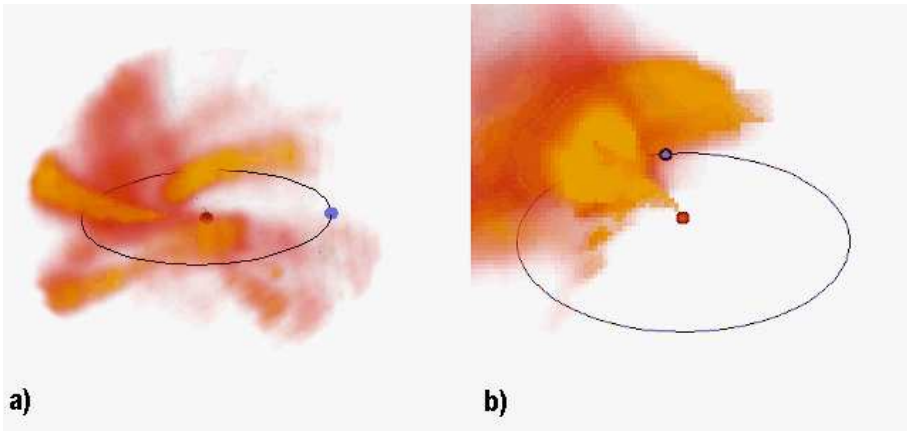

Figure 9. **a)** View of the corotating component of the plasma density in the inner heliosphere (out to 1.5 AU) derived by tomographic reconstruction from IPS intensity level data (Cambridge, UK) and IPS velocity data (Nagoya, Japan) for Carrington rotation 1884 (June 23 to July 20, 1994). The density is normalized by the removal of a r^{-2} distance dependence. The Sun is at the center; the Earth is marked in blue in its orbit around the Sun. The view is from 15° above the plane of the solar equator. The scintillation intensity level is calibrated in terms of density by comparison with IMP spacecraft densities at Earth. Clearly seen is the Archimedean spiral structure of the solar wind (as presented in Jackson *et al.*, 1998). **b)** A three dimensional model projection of the heliosphere from an observer's perspective situated at 3 AU, 30° above the ecliptic opposite the position of Earth on July 7 1994. As in **(a)** density is normalized by the removal of an r^{-2} distance dependence. A solar ejection is observed moving outward to the west of the Sun as seen from Earth.

The first IPS data used in the corotating and time-dependent tomography were combinations of Cambridge, England and STELab IPS velocity data. These data form the basis for the analyses shown in Figure 9a (from Jackson *et al.*, 1998). The same time interval from Carrington rotation 1884 during the year 1994 is reconstructed in both of these analyses. In the corotational analyses that assumes an unchanging source surface with time there are clear discrepancies noted (see Jackson *et al.*, 1998) that could be better dealt with if the model were allowed to evolve with time. Indeed, when the time-dependent tomography began to work both corotating structures and CMEs (see Figure 9b) were observed in the models. Unfortunately, during these time periods no space-based coronagraph was operating to certify the CME shapes in the lower corona. It wasn't until after the Cambridge array was closed in September 1994 that the LASCO coronagraphs on SOHO began operation.

The STELab IPS observations are available during periods when the LASCO coronagraphs operate, and at the best of times the 40 or sources

per day that these radio telescopes observe are sufficient to reconstruct a global model daily using the time-dependent tomography. Figure 10a shows a LASCO C2 coronagraph image of the July 11 halo CME compared with a remote observer view of the modeled tomographic density as the CME is about to reach 1 AU. The reconstruction shows that this CME moves mostly to the east and north of the Earth as also indicated in the coronagraph image. Similarly, Figure 10b shows the Bastille-day CME compared with a remote observer view of the reconstructed density as the CME is about to hit Earth. Given the expanse of heliosphere that the CMEs have traversed to reach 1 AU, the comparisons with LASCO near-Sun observations are excellent. The results of the present three-dimensional reconstruction are in good agreement for the Bastille-day CME with an alternate reconstruction analysis by Tokumaru *et al.* (2002).

The *Helios* Thomson scattering time-dependent tomography also gives excellent agreement with Solwind coronagraph observations in 1979 where these two sets of data exist simultaneously. The major structure observed in Figure 11a is a coronal mass ejection that was observed by the Solwind coronagraph (Poland *et al.*, 1981) to arise from the Sun to the solar northwest at midday 7 May, 1979. This well-studied CME (Jackson and Leinert, 1985; Jackson, 1985; Jackson, Rompolt, and Svestka, 1988; Jackson and Froehling, 1995) was termed "three-pronged" by the Solwind coronagraph group. At the time of Figure 11b the front portion of the CME is estimated to have a solar distance of at least 1.0 AU (Jackson, Rompolt, and Svestka, 1988). This compares with the shape of the outer portion of this CME obtained by the two-spacecraft tomographic reconstruction technique (Jackson and Froehling, 1995). This is the same time period in May, 1979 as shown in the *in situ* data comparison in the last section. In both 3-D reconstruction techniques, the northern portion of the CME is directed away from Earth and northerly while the southern feature is directed primarily northwest of the Sun-Earth line. The 1979 time period during Carrington rotation 1681 is at the extreme maximum of CME activity for Solar Cycle 21. Far more CMEs can be observed throughout this period and related to CMEs observed by the Solwind coronagraph, and some of these CMEs and CME sequences are far more extensive than the single isolated 7 May CME. In particular this is the case with a CME that erupted from the Sun on 25 May 1979 that has also been reconstructed by both the two-spacecraft (Jackson and Hick, 1994) and single spacecraft reconstruction techniques.

Although no coronagraph data exist during the period in November 1977 shown in Figure 12a the period has been well studied using *in situ* data from 5 different spacecraft (Burlaga *et al.*, 1980). Figure 12b is a

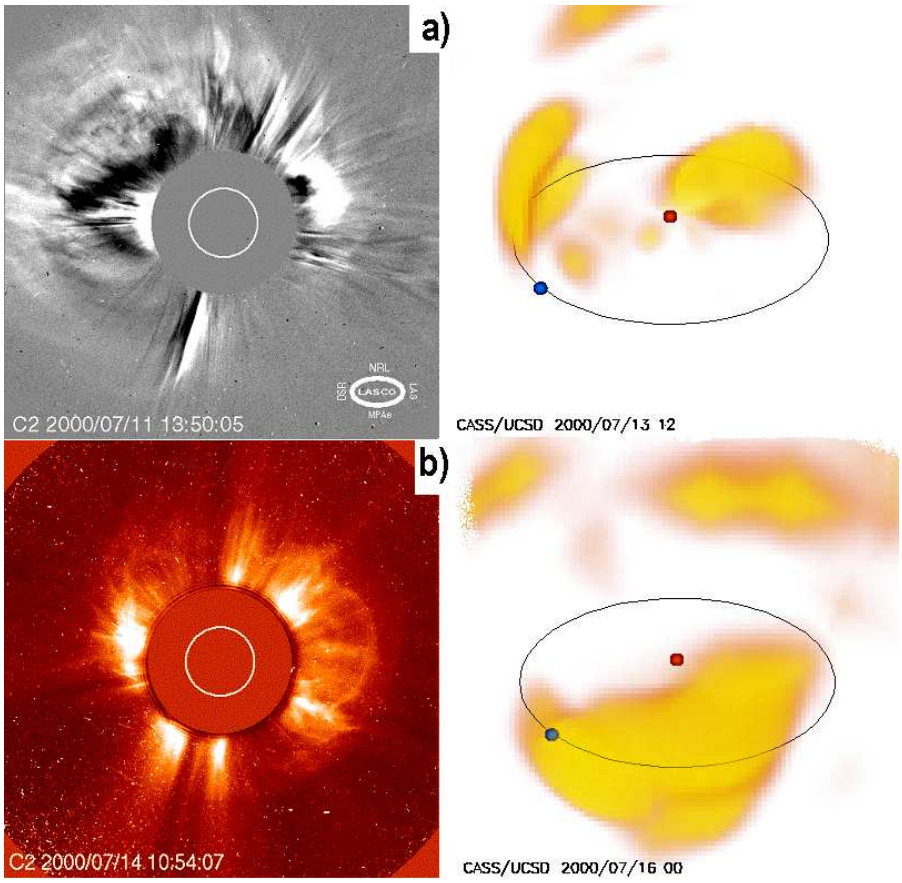

Figure 10. LASCO C2 images and a view of the reconstruction of the halo CMEs in July, 2000 with Ne ¿30e-cm-3 normalized to 1 AU shown. Views (left to right) are 3° across from 1 AU; 55° across from 3 AU, 30° above the ecliptic plane 45° west of the Sun-Earth line. **a)** July 11, 2000 CME in LASCO reconstructed July 13 at 12 UT. **b)** July 14 CME in LASCO reconstructed July 16 at 0 UT.

remote observer view of the *Helios* data at this same time period. The *Helios* photometer time-dependent tomographic model density satisfactorily depicts both the corotating structure and the assumed CME piston that were postulated using *in situ* observations.

More precise measurement of these global models is possible by forming a Carrington map surface at a constant solar height and providing a contour plot of the model at this height. Figure 13 shows two Carrington contour maps of velocity and two of density during the July 11-14 CME sequence from the time-dependent tomography model. The heights and times chosen show the model density when the front

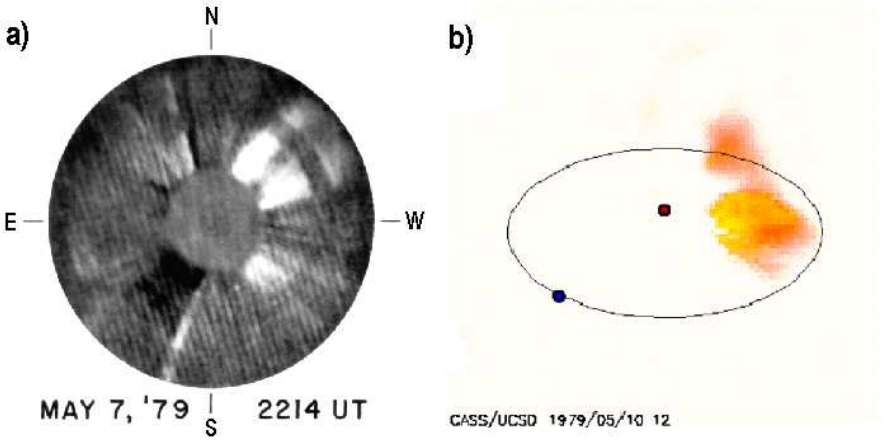

Figure 11. **a)** Solwind coronagraph image of the 7 May CME observed at the time indicated. The coronagraph outer field of view extends to 8 RS. **b)** Remote observer view of heliospheric density at the time indicated. An $r^{-2.07}$ density gradient fit to the observations over the Carrington rotation 1681 interval has been removed from the kinematic model ambient (fit from *Helios* 2 *in situ* measurements at 7.0 e− cm−2 at 1 AU), and to the reconstructed structures to aid in viewing them. The observer is located at 3.0 AU 30° above the ecliptic plane ∼ 45° west of the Sun-Earth line.

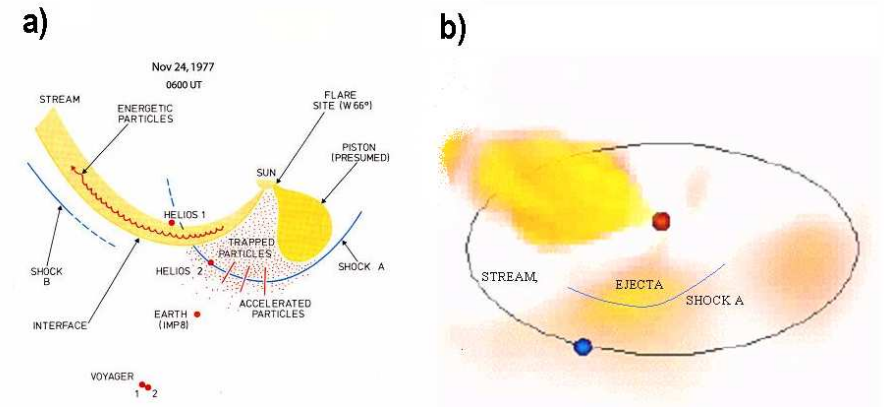

Figure 12. Nov 24, 1977 reconstruction at 6 UT. **a)** using *in situ* observations from 5 spacecraft (Burlaga *et al.*, 1980). **b)** Using the IPS time-dependent Thomson scattering tomography.

portions of the disturbances reach 1 AU at 12 UT on July 13, 2000 and at 0 UT July 16, 2000. Velocities are shown at these same times at a solar distance of 0.3 AU. We have purposely chosen these times to demonstrate one aspect of the observations - namely that both of the reconstructed disturbances show a high velocity region centered below the disturbance and filling in below the disturbance with a following high-speed wind. The high speed wind fills in behind the CME at ever increasing longitude consistent with a source region that temporarily rotates with the solar surface. This region is larger and higher-speed in the case of the July 14 event. These high velocity plumes were first noticed in the time-dependent tomographic analyses, and are either associated with the transient coronal holes studied by others (*e.g.*, Rust, 1983) as a dimming in Yokoh spacecraft X-ray or EIT data or else are associated with reconnection following a CME (Riley *et al.*, 2002), or both. Each high velocity plume has some structure, is generally small compared with the size of the major disturbance that proceeds it into the heliosphere, and appears following most CME disturbances viewed to date with the approximate location and orientation of the solar surface dimming following a CME. In any case these transient high velocity plumes are uniquely present only in the velocity IPS time-dependent tomography.

For the *Helios* spacecraft photometer volume for the CME of May 7, 1979 we show a Carrington map on 12 UT 10 May, 1979 in Figure 14 at the same time as the remote view of Figure 11. Poland *et al.* (1981) estimate that this CME had an excess mass of 10^{16}g assuming that its entire excess mass was located in the plane of the sky observed by Solwind. The CME underwent considerable evolution by the time it reached the *Helios* viewing position, expanding both outward and in north-south size. By summing over time and space in the 3-D matrix using the current tomographic reconstruction, this CME is estimated to have an excess mass of $\sim 4 \times 10^{16}$g at 1.0 AU. If the total CME mass above zero within the CME volume is included, the CME mass is estimated to be $\sim 1 \times 10^{17}$g and the CME takes from 18 UT 9 May to 18 UT 13 May, 1979 to completely pass 1 AU! This compares with values of 6×10^{15}g and 9×10^{15}g respectively for the outer portion of this CME obtained by the two-spacecraft tomographic reconstruction technique (Jackson and Froehling, 1995).

The time interval depicted on 6 UT 24 November, 1977 in Figure 12 is shown as a Carrington synoptic map at 0.6 AU slightly following that time at 12 UT 25 November, 1977 in Figure 15. A shock observed *in situ* at *Helios* was observed to pass both spacecraft about one day earlier than the time of this synoptic map. The density enhancement reconstructed in the tomographic model in this synoptic map is approx-

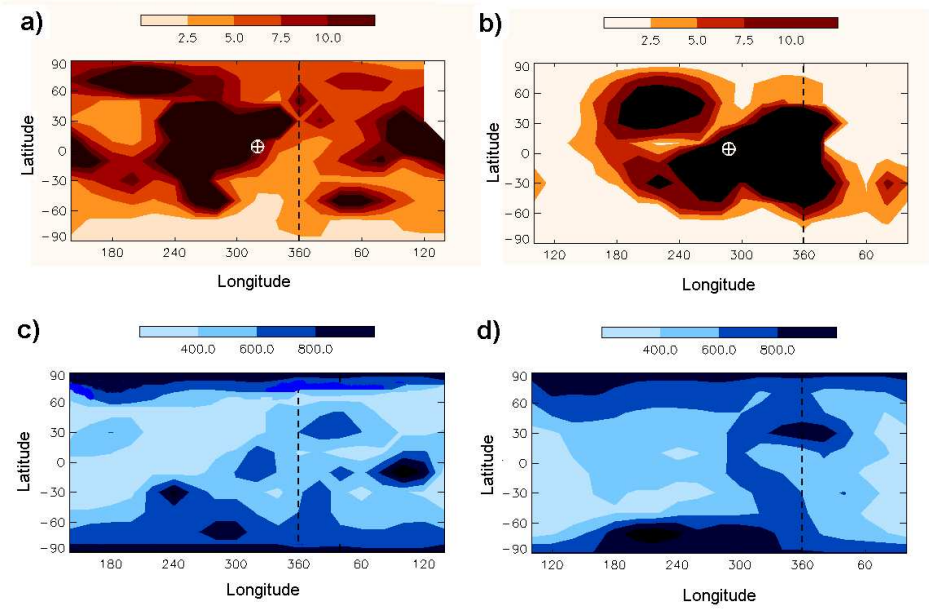

Figure 13. Carrington synoptic maps of time periods during the two halo CMEs in July, 2000. Density maps and are presented at 1.0 AU, velocity maps are presented at 0.3 AU for the same time interval for each event. The Earth ⊕ is centered in each 1.0 AU density map. Both reconstructions are at the same time as the remote observer views in Figure 10. The **a)** density and **c)** velocity maps of the July 11, 2000 CME are shown on July 13 at 12 UT. The CME density is centered at latitude 270° longitude 20°N latitude in the maps. The high speed velocity beneath the CME is centered at 320° longitude at the same latitude. The **b)** density and **d)** velocity maps of the July 14, 2000 CME are shown on July 16 at 0 UT. The CME density is centered at latitude 330° longitude 0° latitude. The high speed velocity beneath the CME is centered at 360° longitude and 30°N latitude.

imately consistent in location with the *in situ* enhancment observed following the shock front.

5. Conclusion

The tomographic analysis handles density both nearby and distant from the spacecraft as accurately as the modeling and data precision allows. From comparison with *in situ* data at Earth, and at the *Helios* spacecraft the time-dependent tomographic analysis (Jackson, Buffington, and Hick, 2001; Jackson, Hick, and Buffington, 2002) gives superior results to the previous corotating analyses (Jackson *et al.*, 1998; Kojima *et al.*, 1998), but only when the data are precise and

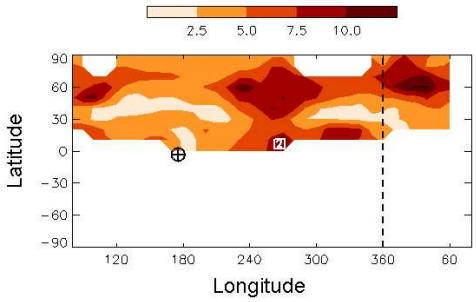

Figure 14. Carrington synoptic map of the heliospheric structure at 1.0 AU on 12 UT 10 May 1979. At this time the *Helios* 2 spacecraft is $\sin 90°$ west of Earth in heliographic longitude (centered as indicated) at a solar distance of 0.3 AU. The Earth $\oplus$ is shown to the left near 180° in the 1.0 AU density map.

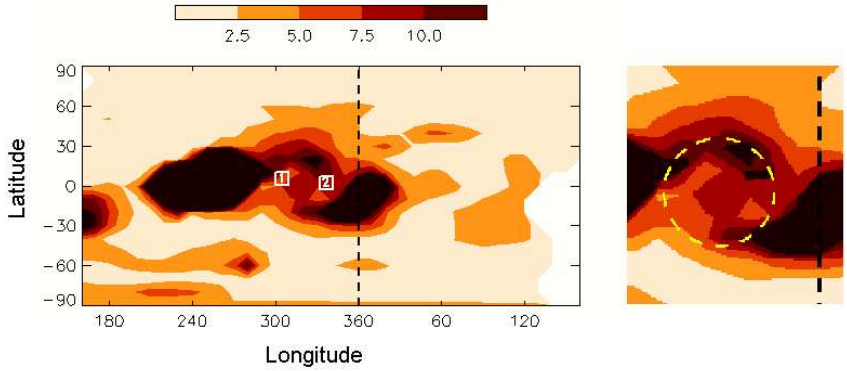

Figure 15. Carrington synoptic map of the heliospheric structure at 0.6 AU on 12 UT 25 November, 1977. The positions of the two *Helios* spacecraft at 0.69 (*Helios* 1) and 0.64 AU (*Helios* 2) are indicated on the full map that shows that the primary dense structure at this time in the ascending phase of the solar cycle is centered around the solar equator. An enlargement at the right of the center of the map shows a ring-like structure that is approximately 40° in size centered between the two *Helios* spacecraft.

quantitative-enough to warrant the necessary degradation in spatial resolution needed to insure convergence. We reconstruct as complete as possible a global three-dimensional model in order to obtain a good fit to observations at Earth, even though these global models amount to only a few tens of lines of sight per day. In real-time analysis, data dropouts and noise make the task of forecasting CME arrival using this technique with the present STELab arrays even more problematic.

We currently operate these two tomographic reconstruction techniques in near real time using IPS observations from STELab, Japan. Since July, 2002, when the IPS array telescopes are operating, all the major CMEs observed by the LASCO coronagraphs (Rappoport, Hick, and Jackson, 2003) have been seen in the IPS data, and the tomography can determine their approximate three-dimensional extents as they move outward into the heliosphere. However, we expect that only when new and bigger IPS systems are available will the IPS technique enbable a sufficiently-refined tomographic analysis to accurately forecast CME arrival to within a few hours. Other large array systems at different Earth longitudes will also be helpful, since coverage using a single IPS array system can obviously only view heliospheric structures heading towards the Earth when it can view sources near the Sun. At any one Earth longitude this observation period is limited to a few hours around local noon. The Solar Mass Ejection Imager (SMEI) (Jackson, *et al.*, 1989; Jackson, Gold, and Altrock, 1991; Jackson, *et al.*, 1992; 1996; Keil *et al.*, 1996a; 1996b; Jackson *et al.*, 1997a) will theoretically be able to reconstruct density over the entire heliosphere with approximately $1^\circ \times 1^\circ$ heliospheric latitude-longitude spatial resolution and a 90-minute temporal cadence. Near the Earth the SMEI data with updates every 100 minute orbit can revise a real time density forecast at Earth so that accuracy at Earth's position can be maintained. However, the SMEI analyses alone cannot as completely determine the velocities required to complete a global solar wind model and only velocity information such as available from the IPS velocity measurements can do this in order to help complete the SMEI far-field view.

Thus, we expect that by using SMEI analyses alone the structures near the Earth can be more accurately reconstructed in density than can those more distant from it. Other spacecraft instruments such as those on board STEREO may operate during the same times as SMEI. If so these other instruments may help fill in heliospheric regions not observed well from the SMEI spacecraft or from ground-based IPS observations and provide far more information about plasma structures in regions of the heliosphere distant from Earth.

The kinematic model currently fit by the tomography can be improved significantly by using a technique whereby the boundary condition (source surface) for a 3D-MHD model is adjusted to give a best fit to the three-dimensional tomographic analysis. One such attempt has been pioneered for corotating tomography by Hayashi *et al.*, 2002. We have our own procedure to incorporate any heliospheric MHD model into our analysis, but these are not needed for forecast purposes until global data become more numerous and precise.

Acknowledgements

The work of B.V. Jackson and P.P Hick was supported at the UCSD by AFOSR grant AF49620-01-1-0054, NSF grant ATM 98-199947 and NASA grant NAG5-8504.

References

Anderson, D.L., and Dziewonski, A.M.; 1984, *Sci. Am.*, **251(4)**, 60.
Allen, C.W.: 1964, Astrophysical Quantities, Athlone, London.
Anzer, U: 1978, *Solar Phys.*, **57**, 111.
Asai, K., Kojima, M., Tokumaru, M., Yokobe, A., Jackson, B.V., Hick, P.L., and Manoharan, P.K.: 1998, *J. Geophys Res.*, **103**, 1991.
Behannon, K.W., Burlaga, L.F., and Hewish, A.: 1991, *J. Geophys. Res.*, **96**, 21213.
Billings, D.E.: 1966, *A Guide to the Solar Corona*, p. 150, Academic, New York.
Bougeret, J.L., King J.H., and Schwenn, R.: 1984, *Solar Phys.*, **90**, 401.
Bracewell, R.N.: 1956, *Australian J. Phys.*, **9**, 198.
Burlaga, L., Lepping, R., Weber, R., Armstrong, T, Goodrich, C., Sullivan, J., Gurnett, D., Kellogg, P., Keppler, E., Mariani, F., Neubauer, F., Rosenbauer, H., and Schwenn, R.: 1980, *J. Geophysical Res.*, **85 (A4)**, 2227.
Chapman, R,W.: 1979, *Sky and Telescope*, **58 (3)**, 223.
Coles, W. A., and Kaufman, J.J.: 1978, *Radio Science*, **13**, 591.
Coles, W. A., Rickett, B.J., Rumsey, V.H., Kaufman, J.J., Turley, D.G., Anathakrishnan, S., Armstrong, J.W., Harmon, J.K., Scott, S.L., and Sime, D.G.: 1980, *Nature*, **286**, 239.
Crifo, F., Picat, J.P., and Cailloux, M.: 1983, *Solar Phys.*, **83**, 143.
Frazin, R.A.: 2000, *Astrophys. J.*, **530**, 1026.
Frazin, R.A., and Janzen, P.: 2002, *Astrophys. J.*, **570**, 408.
Frey, S., Frey, H.U., Barnes, O.H., and Haerendel, G.: 1996, *J. Geophys. Res.*, **101**, 21731
Gapper, G.R., Hewish, A., Purvis, A., and Duffet-Smith, P.J.: 1982, *Nature*, **296**, 633.
Garcia, F.J., Taylor, M.J., and Kelley, M.C.: 1997, *Applied Optics*, **36**, 7374.
Gies, D., Fullerton, A.W., Boulton, C.T., Bagnuolo, W.G., Jr., Hahula, M.E., and Wiemker, R.: 1994, *Astrophys. J.*, **422**, 823.
Gilbert, P.: 1972, *J. Theor. Biol.*, **36**, 105.
Goldstein, B.E., Buffington, A., Cummings, A.C., Fisher, R., Jackson, B.V., Liewer, P.C., Mewaldt R.A., and Neugebauer, M.: 1998, *Proc. SPIE* **3442**, 65.
Gorbunov, M.E.: 1996, *Radio Sci.*, **31(1)**, 95.
Hayashi, K., Fujiki, K., Kojima M., and Tokumaru, M.: 2002, in *Solar Wind 10*, June 17-21, 2002, Pisa, (in press).
Hewish, A., Scott, P.F., and Wills, D.: 1964, *Nature*, **203**, 1214.
Hewish, A., and Bravo, S.: 1986, *Solar Phys.*, **106**, 185.
Hick, P.P., Jackson, B.V. and Buffington, A.: 2000, *BAAS*, **32**, 1488.
Hick, P., Jackson, B.V., Rappoport, S., Woan, Slater, G., Strong, K., and Uchida, Y.: 1995, *Geophys. Res. Lett.*, **22**, 643.
Hurlburt, E., Martens, C.H., Slater, G., and Jaffey, S.M.: 1994, in *Solar Active Region Evolution: Comparing Models With Observations, ASP Conf. Ser.*, **68**, Balasubramaniam, K.S., and Simon, G.W., eds., p. 30.

Hoeksema, J.T., Wilcox, J.M., and Scherrer, P.H.: 1983, *J. Geophys. Res.*, **88**, 9910.
Houminer, Z., 1971, *Nature Phys. Sci.*, **231**, 165.
Houminer, Z., and Gallager, F.: 1993, *Sol. Phys.*, **145**, 359.
Hundhausen, A.J., Bame, S.J., Ashbridge, J.R., and Sydoriak, S.J.: 1970, *J. Geophys. Res.*, **75**, 4643.
Jackson, B.V.: 1977, in a Topical Conference on Solar and Interplanetary Physics, Tucson, Arizona, January 12-15, 7.
Jackson, B.V.: 1985, *Solar Phys.*, **100**, 563.
Jackson, B.V.: 1991, *J. Geophys. Res.*, **96**, 11,307.
Jackson, B.V., and Leinert, C.: 1985, *J. Geophys. Res.*, **90**, 10,759.
Jackson, B.V., and Hick, P.L.: 1994, in the Third SOHO Workshop, Solar Dynamic Phenomena and Solar Wind Consequences, *ESA SP-373*, 199.
Jackson, B.V., and Froehling, H.R.: 1995, *Astron. Astrophys.*, **299**, 885.
Jackson, B.V., and Hick, P.: 2000, *Advances Space Res.*, **25 (9)**, 1875.
Jackson, B.V., and Hick, P.P.: 2002, *Solar Phys.*, **211**, 344.
Jackson, B.V., Rompolt, B., and Svestka, Z.: 1988, *Solar Phys.*, **115**, 327.
Jackson, B., Gold, R., and Altrock, R.: 1991, *Adv. Space Res.* **11**, 377.
Jackson, B.V., Buffington, A., and Hick P.P.: 2001, in the Proc. of "Solar Encounter: The First Solar Orbiter Workshop", *ESA SP-493*, 251.
Jackson, B.V., Hick, P.P., and Buffington, A.: 2002, in *S.P.I.E. proc.* **4853**, 23.
Jackson, B.V., Howard, R.A., Sheeley, N.R., Jr., Michels, D.J., Koomen, M.J., and Illing, R.M.E.: 1985, *J. Geophys. Res.*, **90**, 5075.
Jackson, B.V., Hudson, H.S., Nichols, J.D., and Gold, R.E.: 1989, Waite J.H., Jr., Burch J.L., and Moore, R.L., eds., *Geophysical Monograph* **54**, 291.
Jackson, B.V., Webb, D.F., Altrock R.C., and Gold, R.: 1992, *Eruptive Solar Flares* Svestka, Z., Jackson, B.V., and Machado M.E., (eds.), Springer-Verlag, Heidelberg, 322.
Jackson, B.V., Buffington, A., Hick, P.L., Kahler, S.W., Altrock, R.C., Gold, R.E., and Webb, D.F.: 1996, in D. Winterhalter, J.T. Gosling, S.R. Habbal, W.S. Kurth, and M. Neugebauer (eds.), *Solar Wind Eight*, AIP Conf. Proc. 382, Woodbury, New York, p. 536.
Jackson, B.V., Buffington, A., Hick, P., Kahler, S.W., Keil, S.L., Altrock, R.C., Simnett, G.M., and Webb, D.F.: 1997a, *Phys. Chem. Earth*, **22**, 441.
Jackson, B.V., Hick, P.L., Kojima M., and Yokobe, A.: 1997b, *Adv. Space Res.*, **20**, (1), 23.
Jackson, B.V., Hick, P.L, Kojima, M., and Yokobe, A.: 1998, *J. Geophys. Res.*, **103**, 12,049.
Jackson, B.V., Hick, P.P., Buffington, A., Kojima, M., Tokumaru, M., Fujiki, K., Ohmi T., and Yamashita, M.: 2002, in *Solar Wind 10*, June 17-21, 2002, Pisa, (in press).
James, J.F., Mukai, T., Watanabe, T., Ishigura, M., and Nakamura, R.: 1997, *Mon Not. R. Astron. Soc.*, **288**, 1022.
Katz, M.B.: 1978, *Lecture Notes in Biomathematics*, **26**, Levin, S., ed., Springer-Verlag, New York.
Kakinuma, T.: 1977, in *Study of Traveling Interplanetary Phenomena*, Shea, M.A., Smart, D.F., and Wu, S.T., eds., D. Reidel, Norwell, Mass.,101.
Keil, S.L., Altrock, R.C., Kahler, S., Jackson, B.V., Buffington, A., Hick, P.L., Simnett, G.M., Eyles, C.J., Webb, D., and Anderson, P.: 1996a, *S.P.I.E. proc.*, **2804**, 78.
Keil, S.L., Altrock, R.C., Kahler, S.W., Jackson, B.V., Buffington, A., Hick, P.L., Simnett, G., Eyles, C., Webb, D.F., and Anderson, P.: 1996b, in Solar Drivers of

Interplanetary and Terrestrial Disturbances, Balasubramaniam, K.S., Keil S.L., and Smartt R.N., eds., *ASP Conference Series*, **95**, 158.
Kojima, M., and Kakinuma, T., 1987, *J. Geophys. Res.*, **92**, 7269.
Kojima, M., and Kakinuma, T.: 1990, *Space Sci. Rev.*, **53**, 173.
Kojima, M., Asai, K., Hick, P.L., Jackson, B.V., Tokumaru, M., Watanabe, H., and Yokobe, A.: 1997, in S.R. Habbal (ed.), Robotic Exploration close to the Sun: Scientific Basis, *AIP Conference Proceedings 385*, 97.
Kojima, M., Tokumaru, M., Watanabe, H., Yokobe, A., Asai, K., Jackson, B.V., and Hick, P.L.: 1998, *J. Geophys. Res.*, **103**, 1981.
Leinert, Ch., and Jackson, B.V.: 1998, *Astrophys. J.*, **505**, 984.
Leinert, C., Link, H., and Salm, N.: 1981, *J. Space Sci. Instr.*, **5**, 257.
Leinert, C., Link, H., Pitz, E., Salm, N., and Knuppelberg, D.: 1975, *Raumfahartforschung*, **19**, 264.
Leinert, C., Richter, I., Pitz, E., and Planck, B.: 1981, *Astron. and Astrophys.*, **103 (1)**, 177.
McComas, D.J., Phillips, J.L., Bame, S.J., Gosling, J.T., Goldstein, B.E., and Neugebauer, M.: 1995, *Space Sci. Rev.*, **72**, 93.
MacQueen, R.M.: 1993, *Solar Phys.*, **145**, 169.
Marsh, T.R., and Horne, K.; 1988, *Mon. Not. R. Astron.. Soc.*, **235**, 269.
Mouschovias, T., and Poland, A.I.: 1978, *Astrophys. J.*, **220**, 675.
Munro, R.H.: 1977, in Topical Conference on Solar and Interplanetary Physics, Tucson, Arizona, January 12-15, 10.
Panasyuk, A.V.: 1999, *J. Geophys. Res.*, **104**, 9721.
Poland, A.I., Howard, R.A., Koomen, M.J., Michels, D.J., and Sheeley, N.R., Jr,: 1981, *Solar Phys.*, **69**, 169.
Rappoport, S., Hick, P.P., and Jackson, B.V.: 2003, *BAAS*, **34 (4)**, 1242.
Richter, I., Leinert, C., and Planck, B.: 1982, *Astron. Astrophys.*, **110**, 115.
Riley, P., Linker, J.A., Mikic, Z., Odstrcil, D., Pizzo, V.J., and Webb, D.F.: 2002, *Astrophys. J.*, **578**, 972.
Rust, D.M.: 1983, *Rev. Geophys. Space Phys.*, **21(2)**, 349.
Schwenn, R.: 1990, in R. Schwenn and E. Marsch (eds.), *Physics of the Inner Heliosphere, 1*, Springer-Verlag, Berlin, Germany, p. 99.
Tatarski, V.I.: 1961, *Wave propagation in a turbulent medium*, McGraw-Hill, New York.
Tokumaru, M., Kojima, M., Fujiki, M., and Yamashita, M.: 2002, in *Solar Wind 10*, June 17-21, 2002, Pisa, (in press).
Young, A.T.: 1971, *Astrophys. J.*, **168**, 543.
Wilson, D.C.: 1977, NCAR Cooperative Thesis No. 40, Ph.D. thesis to the University of Colorado, Boulder, Colorado.
Worcester, P., Corunelle, B.D., and Spindel, R.C.; 1991, *U.S. Natl. Rep. Int. Union Geod. Geophys. 1987-1991, Rev. Geophys.*, **29**, 557.
Wu, S.T., Dryer, M., and Han, S.M.; 1976, *Sol. Phys.*, **49**, 187.
Zidowitz, S., Inhester, B., and Epple, A.: 1995, in D. Winterhalter, J.T. Gosling, S.R. Habbal, W.S. Kurth, and M. Neugebauer (eds.), *Solar Wind Eight*, AIP Conf. Proc. 382, Woodbury, New York, p. 165.